

Graphical Abstract

Fully Vectorized Linear Operator Formulation for Inverse Scattering Problems

R. G. Wueest, J. Mueller, J. Aichele, H. R. Thomsen

Highlights

Fully Vectorized Linear Operator Formulation for Inverse Scattering Problems

R. G. Wueest, J. Mueller, J. Aichele, H. R. Thomsen

- Presents a fully vectorized linear operator framework for inverse scattering in NDT.
- Relies solely on the principles of linear time-invariant (LTI) systems, avoiding the need for theoretical assumptions about wave propagation.
- Enforces periodic discrete time, enabling FFT-diagonalizable circular convolution operators which are solvable using the Tikhonov regularized inverse.
- Localizes sub-wavelength sized defects in both simulated aluminum plates and real-world CFRP plates.
- Post-calibration, only sparse sensor measurements are needed for rapid health monitoring.

Fully Vectorized Linear Operator Formulation for Inverse Scattering Problems

R. G. Wueest^{a,*1} (Researcher), J. Mueller^b (Advisor), J. Aichele^b (Advisor) and H. R. Thomsen^{b,2} (Advisor)

^aDepartment of Physics, ETH Zürich, 8092, Zürich, Switzerland

^bDepartment of Earth Sciences, ETH Zürich, 8092, Zürich, Switzerland

ARTICLE INFO

Keywords:

inverse scattering
non-destructive testing
ultrasonic NDT
defect localization
empirical impulse response
Tikhonov regularization
structural health monitoring

ABSTRACT

We present an empirical, fully vectorized linear-operator framework for inverse scattering and validate it experimentally on a bidirectional carbon-fiber-reinforced polymer (CFRP) plate. The framework uses bonded piezoelectric transducers to emit periodic pulses and a Laser Doppler Vibrometer (LDV) for a one-time calibration scan, constructing source–receiver impulse-response operators. By enforcing a discrete, periodic time behavior, wave propagation is modeled as circular convolution, diagonalizable via the discrete Fourier transform (DFT). Defect localization is formulated as a Tikhonov-regularized linear inverse problem.

After calibration, monitoring uses only sparse measurements at the transducer locations. An iron cube glued to the plate serves as a defect proxy and is localized to a sub wavelength resolution. Computation is concentrated in the one-time calibration; subsequent evaluations require minimal data and time. Long-term, transducer-only calibration could enable fully automated structural health monitoring, and the empirical-operator concept may extend to alternative detection systems or unconventional sensing interfaces (e.g., touch-like surfaces). The approach is model-free and broadly applicable where forward modeling or digital-twin upkeep is impractical.

1. Introduction

Structural Health Monitoring (SHM) of engineered components aims to localize and characterize defects. The importance of SHM depends on the cost of failure, which is especially relevant in aviation, hence many methods of performing SHM on flat structures have been explored and documented. Among these methods, Piezoelectric sensors are promising from a commercial point of view due to their low cost. However, increased challenges are noted when monitoring CFRP components [4]. Different state of the art Methods for CFRP specifically are explored in [3].

Sparse monitoring using Piezoelectric sensors (measuring at a few strategically placed sensors) would be therefore be especially desirable, but it typically demands detailed numerical forward models that are difficult to build and maintain in composites [6]. Carbon-fiber-reinforced polymer (CFRP) plates, in particular, exhibit variability from layup and manufacturing that undermines predictive digital twins [1].

This paper validates a model-free alternative based on empirical linear operators and a fundamentally periodic time embedding. We excite the structure with bonded piezoelectric transducers and use a Laser Doppler Vibrometer (LDV) to perform a dense, one-time calibration scan that constructs source–receiver impulse-response operators. Propagation is treated on a discrete cyclic time axis so that it acts as circular convolution, diagonalized by the discrete Fourier transform (DFT). By designing the excitation to be strictly periodic and ensuring no other sources act on the object, the cyclic time embedding is valid by construction; we impose time periodic behavior in the setup, and thus the frequency treatment becomes equivalent to the time domain treatment. Within a single-scattering formulation, defect localization is solved via Tikhonov-regularized inverse[5] using only sparse monitoring data at the transducer locations.

We validate the approach experimentally on an anisotropic CFRP plate, demonstrating sub-wavelength localization from sparse measurements.

* wueestg@ethz.ch (R.G. Wueest); thomsenh@ethz.ch (H.R. Thomsen)
ORCID(s):

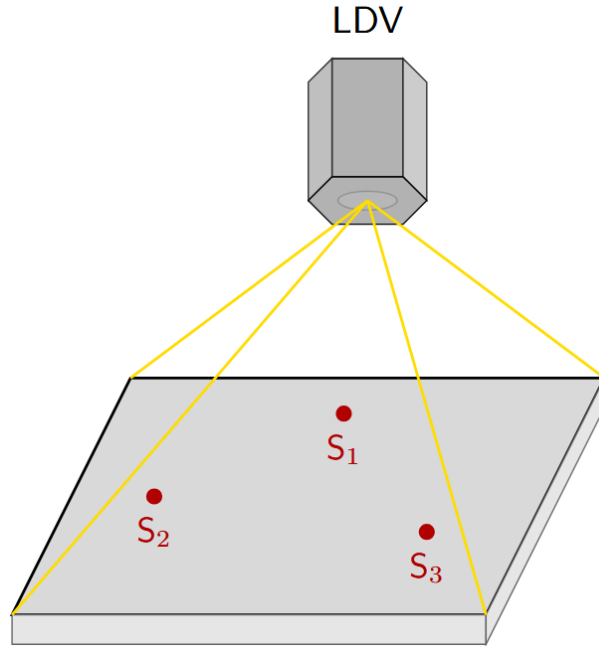


Figure 1: Experimental setup: periodic excitation with a single active transducer; an LDV scans the plate to build empirical source-receiver operators during calibration. The source pulse is taken as the self-measured excitation (including local reverberations), and periodic timing is enforced by design.

2. Methodology

The test specimen is a $25\text{ cm} \times 25\text{ cm}$ bi-directional CFRP plate, 1.3 mm thick. Five ceramic piezoelectric transducers are bonded to the plate. They are excited using an 80 kHz center-frequency Ricker wavelet pulse. An LDV scans the plate on a 104×104 grid, recording the out-of-plane velocity over time (see Figure 1). Figure 2 shows one frame of such a measurement. This scan is repeated for each of the five transducers; these acquisitions constitute the one-time calibration step.

The transducers are commercially available low-cost brass-ceramic piezoelectric discs with a nominal diameter of 12 mm. The drive is a periodic pulse train with a 2 ms repetition period, using a 80 kHz Ricker wavelet as the pulse shape to enforce timing periodicity. Data are sampled at 625 kHz and low-pass filtered to the 50 kHz prior to operator estimation. Each grid location is acquired with 10 repeats 5 separate times. I.e. we obtain 5 sets of measurements total, each having been averaged 10 times. Transducers were bonded using a hand-applied, temperature-activated adhesive; exact formulation and bond thickness were not recorded. As derived in Section 3.4, the method is independent of the source transfer function, and thus works for a wide range of unknown coupling properties.

After calibration, a 1 cm^3 iron cube is bonded to the plate to simulate a defect. During monitoring, we excite each transducer again but measure only at the transducer locations. In our setup, the LDV acquires these sparse responses at the transducer positions; in principle, the transducers themselves can act as receivers, which could enable fully automated, remote NDT/SHM. This could enable cost-effective, highly frequent SHM for important components at a press of a button. See Appendix A.5 for additional discussion of piezoelectric sensing considerations.

To characterize the plate, we estimate its dispersion. We extract an $x-t$ slice along the axis through the active transducer from Figure 2, window the time axis to exclude edge reflections (Figure 3a), and compute a 2D FFT to obtain the $k-\omega$ spectrum. Selecting the peak-energy wavenumber $k^*(f)$ for each frequency yields the phase velocity $v_p(f) = 2\pi f / k^*(f)$ and wavelength $\lambda(f) = 2\pi / k^*(f)$ (Figure 3b).

Raw data with emitter 5 at time 0.17 ms

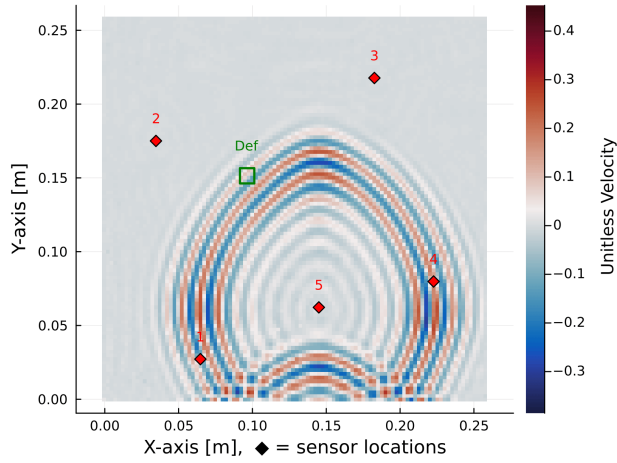
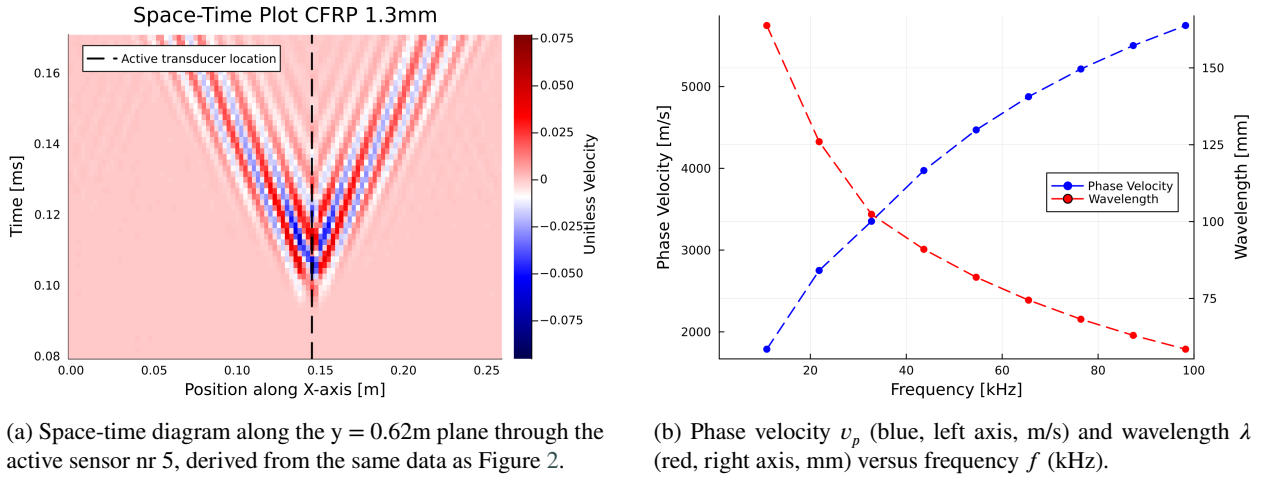


Figure 2: Snapshot of the CFRP plate at $t = 0.17$ ms, lowpass filtered to 150 kHz. Red diamonds mark the five transducers (numbered 1–5); transducer 5 is the active source. The green square indicates the location where the defect will be bonded in the monitoring phase (not yet present in this calibration scan). Note: The results in this paper employ 1–50 kHz bandpass filtering, which significantly distorts the pulse shape compared to this view; see Appendix A.1.



(a) Space-time diagram along the $y = 0.62$ m plane through the active sensor nr 5, derived from the same data as Figure 2.

(b) Phase velocity v_p (blue, left axis, m/s) and wavelength λ (red, right axis, mm) versus frequency f (kHz).

Figure 3: Empirical dispersion of the CFRP plate from the calibration scan.

3. Mathematical framework

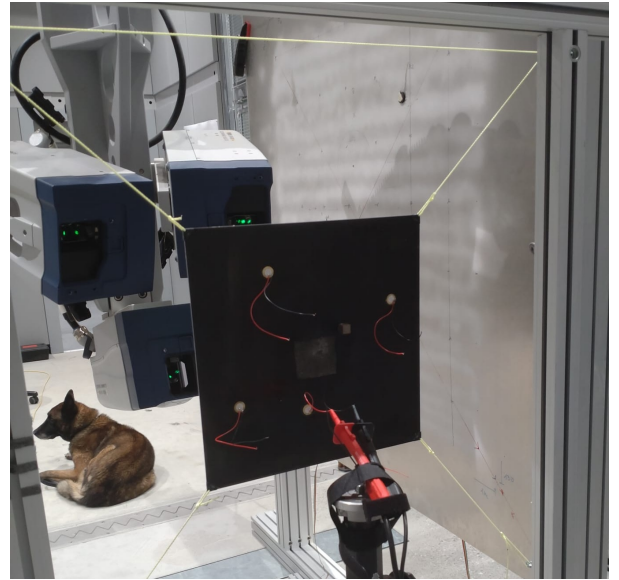
3.1. System assumptions

We assume: (i) linearity; (ii) time invariance; (iii) reciprocity; (iv) practical flatness (LDV access); and (v) the ability to control the excitation of the material relative to noise.

Assumptions (i), (ii), and (iii) are naturally satisfied for mechanical waves under standard conditions. Assumption (iv) refers to geometries where the object thickness is small relative to its lateral dimensions, typically valid for plate-like components such as aircraft fuselage panels and shell structures. Assumption (v) simply requires controlled excitation capability, which is standard in active NDT configurations using piezoelectric or electromagnetic transducers.



(a) LDV setup from the front



(b) LDV Setup from the back

Figure 4: Ich bin mir nicht sicher, ob solche bilder auch enthalten sein sollen, oder eher im Appendix mit verweis? Ein besseres bild von der hinterseite der platte wäre evtl auch noch gut, obwohl ich richtig gerne den Hund drauf behalten würde:D

3.2. Terminology and Notation

We work with discrete-time vectors and matrices throughout. The spatial domain is discretized into a set of points indexed by integers without implying any particular geometric arrangement. For instance, a 100×100 scan grid of a square plate yields 10,000 points labeled 1 through 10,000, with the specific mapping arbitrary, but fixed.

When a transducer emits a signal at location i , represented by time-domain vector \vec{s}_i , the observed signal \vec{m}_j at location j is given by the convolution with the impulse response \vec{g}_{ij} between those locations: $\vec{m}_j = \vec{g}_{ij} * \vec{s}_i$. This formulation separates spatial indices (subscripts) from the time-domain representation (vectors).

For computational implementation, these vectors correspond to discrete-time samples over a fixed acquisition window, with all operations respecting the imposed periodicity described in subsequent sections.

3.3. Periodic time and discrete representation

Repeating the excitations enforces periodicity so that the time axis can be treated on a discrete cyclic domain. Any impulse response between locations i and j is then a circular-convolution operator G_{ij} , represented by a circulant (circular Toeplitz) matrix fully determined by its first column (the sampled impulse-response vector \vec{g}_{ij}). Explicitly, for $\vec{g}_{ij} = (g_0, g_1, \dots, g_{n-1})^T$,

$$G_{ij} = \begin{pmatrix} g_0 & g_{n-1} & \cdots & g_1 \\ g_1 & g_0 & \cdots & g_2 \\ \vdots & \vdots & \ddots & \vdots \\ g_{n-1} & g_{n-2} & \cdots & g_0 \end{pmatrix} \quad (1)$$

so that $G_{ij}\vec{v} = \vec{g}_{ij} * \vec{v}$ (circular convolution). All such operators are diagonalized by the discrete Fourier transform (DFT), enabling component-wise multiplication in frequency.

3.4. Empirical impulse responses

We do not separate an “ideal” injected waveform from local reverberations at a transducer. The self-measured periodic signal \vec{s}_s is taken as the source vector. For a transducer s and measurement point i (grid or other transducer), the response is modeled as a circular convolution:

$$\vec{m}_i = G_{is}\vec{s}_s \quad (2)$$

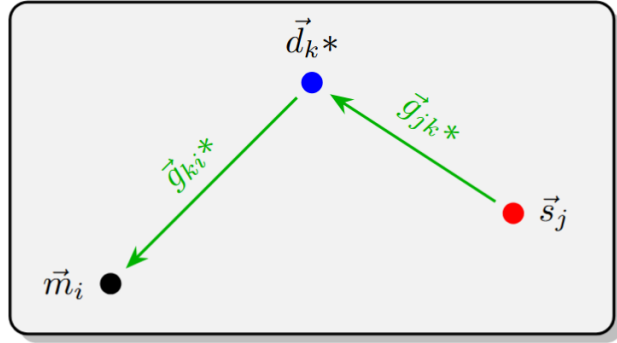


Figure 5: Visualization on how a source at location j propagates to a defect at location k , which then re-emits the wave. Afterwards, it propagates to a receiver location i . As an equation, the image visualizes $\vec{m}_i = \vec{g}_{kj} * \vec{d}_k * \vec{g}_{ik} * \vec{s}_j$.

where G_{is} is circulant (first column \vec{g}_{is}). Directional (mode) decomposition is intentionally omitted because the LDV records only the scalar out-of-plane velocity at each sampled point.

To robustly estimate \vec{g}_{is} , we use repeated measurements. Let $\{(\vec{s}_{s,p}, \vec{m}_{i|s,p})\}_{p=1}^P$ denote P repeated acquisitions. In the frequency domain (hats denote DFT components), for each frequency bin f we solve the Tikhonov-regularized least-squares problem:

$$\min_{\hat{g}_{is}(f)} \sum_{p=1}^P \left| \hat{m}_{i|s,p}(f) - \hat{s}_{s,p}(f) \hat{g}_{is}(f) \right|^2 + \alpha |\hat{g}_{is}(f)|^2 \quad (3)$$

with regularization parameter $\alpha > 0$. The closed-form solution is:

$$\hat{g}_{is}^{\text{reg}}(f) = \frac{\sum_p \overline{\hat{s}_{s,p}(f)} \hat{m}_{i|s,p}(f)}{\sum_p |\hat{s}_{s,p}(f)|^2 + \alpha} \quad (4)$$

The result is a stabilized impulse-response function that does not rely on assuming specific noise characteristics.

Notes: Although the framework is presented with LDV-acquired empirical impulse responses, the same operators G_{ij} can be generated computationally from an analytical model or a digital twin (e.g., FEM/FDTD). In that case, emitter and receiver coupling, as well as the enforced periodicity, must be accounted for separately.

3.5. Defect model

Since defects also satisfy the assumptions in Section 3.1, their effects can be modeled using circular convolutions. Within the single-scattering (Born-type) approximation, the scattering process is illustrated in Fig. 5. For clarity, we first assume a *delta-like* (instantaneous) temporal reflection kernel, so each defect is represented by a scalar amplitude d_k at its spatial location. Algebraically, this corresponds to selecting only the first canonical temporal basis vector \vec{e}_0 . This is a **defect-basis choice** made for pedagogical clarity, not a limitation of the framework. The generalization to richer local bases is presented in Section A.7 after the main operator assembly and inversion.

3.6. Operator assembly

For an emitter at j and a measurement at i , the measured signal consists of a direct propagation term and first-order (single-scattered) contributions, as illustrated in Fig. 5:

$$\vec{m}_i = \vec{g}_{ij} * \vec{s}_j + \sum_{k=1}^N \vec{g}_{ik} * \vec{d}_k * \vec{g}_{kj} * \vec{s}_j. \quad (5)$$

Which can be rewritten in matrix form:

$$\vec{m}_i = G_{ij} \vec{s}_j + \sum_{k=1}^N G_{ik} D_k G_{kj} \vec{s}_j. \quad (6)$$

Using the commutativity of circular convolution, restate the problem as

$$\Delta \vec{m}_{ij} := \vec{m}_i - G_{ij} \vec{s}_j = \sum_{k=1}^N (G_{ik} G_{kj} S_j) \vec{d}_k. \quad (7)$$

Writing the defect vectors \vec{d}_k as a single vector:

$$\vec{\mathbf{d}}_{\text{full}} := \begin{bmatrix} \vec{d}_1 \\ \vec{d}_2 \\ \vdots \\ \vec{d}_N \end{bmatrix} \quad (8)$$

The problem can be restated as a matrix problem with

$$L_{ij}^{\text{gen}} := [G_{i1} G_{1j} S_j \mid G_{i2} G_{2j} S_j \mid \dots \mid G_{iN} G_{Nj} S_j] \quad (9)$$

so that

$$\Delta \vec{m}_{ij} = L_{ij}^{\text{gen}} \vec{\mathbf{d}}_{\text{full}}. \quad (10)$$

This system is typically massively under determined, and even if not too massive for practical computing.

However, knowing that scatterers generally re-emit waves almost immediately, we can restrict the defect vectors \vec{d}_k around a small set of temporal basis functions. As mentioned in the previous section, we continue with the simplest case where $\vec{d}_k = d_k * \vec{e}_0$, i.e., a 1D basis. Since every defect at any location is parameterized by a single parameter d_k , the full defect vector can be represented as

$$\vec{\mathbf{d}} := \begin{bmatrix} d_1 \\ d_2 \\ \vdots \\ d_N \end{bmatrix} \quad (11)$$

and integrated into the problem by including the basis vectors into the problem:

$$L_{ij} := [G_{i1} G_{1j} S_j \vec{e}_0 \mid G_{i2} G_{2j} S_j \vec{e}_0 \mid \dots \mid G_{iN} G_{Nj} S_j \vec{e}_0], \quad (12)$$

where \vec{e}_0 in this equation is to be understood as a column vector. The final problem statement is then

$$\Delta \vec{m}_{ij} = L_{ij} \vec{\mathbf{d}}. \quad (13)$$

Stacking the selected (i, j) pairs yields the global residual system

$$\mathbf{m}_{\text{full}} = L_{\text{full}} \vec{\mathbf{d}}, \quad (14)$$

Here, "stacking" means vertically concatenating the pairwise residual vectors and their corresponding block-row operators, e.g.,

$$\mathbf{m}_{\text{full}} = \begin{bmatrix} \Delta \vec{m}_{12} \\ \Delta \vec{m}_{13} \\ \vdots \end{bmatrix}, \quad L_{\text{full}} = \begin{bmatrix} L_{12} \\ L_{13} \\ \vdots \end{bmatrix}$$

How the stacking is performed in practice depends on how many sensors/emitters are available and how the system is set up.

We have reduced the problem statement to the linear system in (14). The only approximations made are the discretization of space and the assumption of first-order scattering.

3.7. Regularized inversion

Let $\mathcal{L} = L_{\text{full}}$ and $\mathbf{m} = \mathbf{m}_{\text{full}}$. We estimate the defect vector by minimizing the penalized least-squares functional.

$$J(\mathbf{d}) = \|\mathcal{L}\mathbf{d} - \mathbf{m}\|_2^2 + \lambda \|\Gamma^{1/2}\mathbf{d}\|_2^2, \quad (15)$$

where $\Gamma \succeq 0$ specifies the penalty metric (a weighting / masking matrix) and $\lambda > 0$ controls the trade-off between data fit and stabilization. The normal equations yield the closed form

$$\hat{\mathbf{d}} = (\mathcal{L}^T \mathcal{L} + \lambda \Gamma)^{-1} \mathcal{L}^T \mathbf{m}. \quad (16)$$

In practice Γ is diagonal with ones everywhere except zeros at transducer locations along with a small radius around them, so those coefficients are unpenalized. This allows the inversion to self-correct for slight inconsistencies in the emitter pulse form. When plotting the defect vector as a heatmap during evaluation, these regions are omitted from the plot by setting to 0, as otherwise, these regions would dominate the results.

4. Results

Figure 6a shows the reconstructed defect vector $\vec{\mathbf{d}}$, with each pixel representing the absolute value of a spatial grid point. In other words, after solving for the vector $\vec{\mathbf{d}}$ from equation 14, we obtain a vector which for every grid point corresponds to the reflection amplitude of a defect at the given point. In our case, the vector has dimension $101 \times 104 = 10'816$ entries, one parameter per grid point. In order to visualize the data, every grid point is converted back onto the 2D plane based on how it was initially converted onto a 1D system. The absolute value of the index at every grid point is mapped in the final heatmap. This can be interpreted as the amplitude with which the incoming wave is reflected back at each given location, although no information about the phase shift preserves, given the vector is in complex valued. Note that the algorithm itself does not know where every index corresponds to on the 2D plane. Moreover, there is no constraint that the system must be defined over a 2D plane.

The defect in Figure 6a is clearly localized to a small region near the target location (yellow square). A small black region appears around each transducer location (red diamonds); this exclusion zone corresponds to the unpenalized region in the regularization (Section 3.7) and is masked in the visualization. Behind this mask, the heatmap would show very high values for the defect plane, but it mostly corresponds to systematic error in the experiment setup, such as the pulses not having the same amplitude as during calibration.

Figures 6 demonstrates the successful localization of the $1 \times 1 \times 1 \text{ cm}^3$ iron cube using only sparse measurements at the five transducer locations. The particle velocity data was bandpass filtered to the 1–50 kHz range and processed via the Tikhonov-regularized inversion described in Section 3.7.

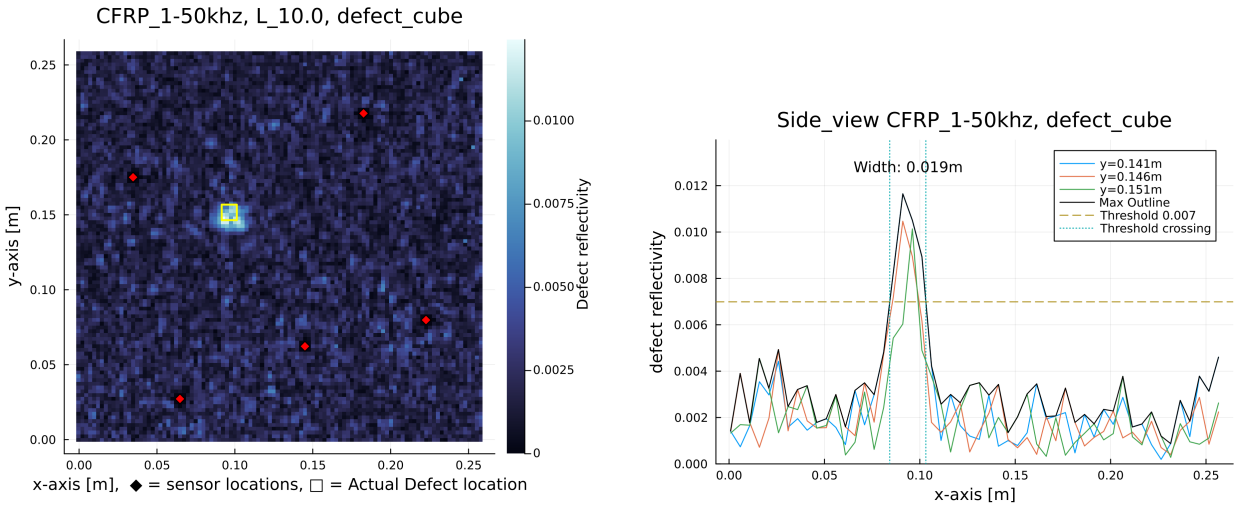
Figure 6b provides cross-sectional views along the x-axis. Slices along x-axis exceeding 0.6 times the maximum amplitude are retained and their envelope is drawn. This threshold identifies the localization width: the defect signature has a half width of approximately 2 cm.

Computations used the 1–50 kHz band exclusively. Testing with extended frequency ranges shows degraded reconstruction quality above 100 kHz.

5. Discussion

The reconstructed defect has a half-width of approximately 2 cm compared to a wavelength of $\lambda_{50} \approx 8 \text{ cm}$ at 50 kHz (Figure 3b), yielding sub-wavelength localization. See Appendix A.3 for further comments regarding the validity of the phase velocities. This is significantly below the wavelength size. This property has garned a large amount of discussions as to why it is the case, and they are hard to answer concisely, as it is hard to show why something is *not* the case. In short, there is no reason why such a restriction should exist given the mathematical methodology used that does not use spatial information. It is easier to point why a given other method *does* have certain restrictions, which usually is caused by the need to reconstruct measured waves in space. [2] is a great example of such a method, that does have the restriction, but does not discuss it.

However, in the simulation study, a decrease in resolution is observed with the lower frequencies, which implies that the method is not completely independent of the wavelength limit. What makes discussion hard however, is that this analysis does not isolate variables; the decrease in the frequency bandwidth simultaneously causes three variables to be changed: Decrease in the maximum frequency, decrease in the amount of information available due to the system



(a) Reconstructed magnitude of the defect vector $|\vec{d}|$ in the 1–50 kHz band. Red diamonds mark the five transducer locations; the yellow square indicates the actual location where the iron cube was bonded. The black regions around transducers are the unpenalized exclusion zones from the regularization.

(b) Cross-sectional profiles along the x-axis through the reconstructed defect (left panel). Colored envelopes show slices with amplitude exceeding 0.6 times the maximum. The localization width is estimated from the 0.6 amplitude threshold, yielding a half-width of approximately 2 cm.

Figure 6: Defect localization results in the 1–50 kHz band using sparse transducer measurements. Left: full 2D reconstruction showing sub-wavelength localization of the defect. Right: cross-sectional analysis quantifying the localization width.

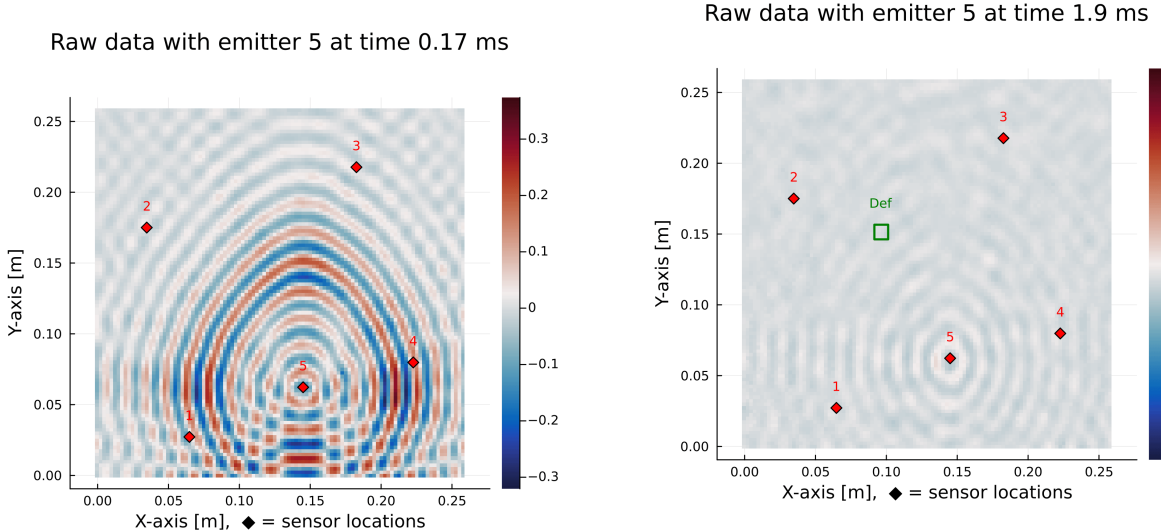
matrix shape 14, and susceptibility to the standard norm based regularization *smearing* the result due to neighboring points having more similar responses as a result of longer wavelengths. For all intents and purposes, the method does have a resolution limitation as a function of frequency, but it is not caused by a hard mathematical limit such as the Nyquist sampling theorem for example, but rather a collection of various limitations. Given the proof of concept nature of this paper, I refrain from digging deeper into this topic, just noting as a closing point that it is possible to isolate each of these variables to obtain definite answers if one so desires.

The unpenalized region around transducers (Section 3.7) was necessary to suppress phantom defects in early inversions. Pulse shape measurements confirmed slight temporal and amplitude variations between calibration and monitoring phases. Rather than correcting these variations explicitly, the inversion absorbs them locally in the unpenalized zones.

Testing with extended frequency ranges showed that the 1–80 kHz band yields only modest quality improvements over 1–50 kHz, while extending to 1–150 kHz causes severe reconstruction degradation. Analysis of the 100–150 kHz band alone yields poor results, indicating that this frequency range carries no useful information for defect localization in the current setup. The 1–50kHz Range working similarly well to 1–80kHz is especially interesting considering the system matrix to be solved in equation 14 has dimensions 1000×10816 . The inversion problem is highly underdetermined by a factor of over 10. Further discussion can be found in Appendix ??.

A key source of degradation at higher frequencies likely is misalignment between the calibration and monitoring phases. During calibration, the LDV scans a dense 104×104 grid. During monitoring, the LDV measures at transducer locations only, and realignment relies on visual cues, introducing small spatial offsets. Such misalignments couple strongly to phase information at shorter wavelengths. Notably, this alignment issue would be eliminated entirely if monitoring were performed using the transducers themselves as receivers rather than the LDV, as discussed in Section A.5. At high frequencies, the Born approximation may also break down as secondary and multiple scattering contributions become more relevant.

The absolute pixel values in Figure 6a should be interpreted as relative indicators of defect location rather than quantitative scattering amplitudes. Regularization parameter λ significantly influences amplitude scaling, and the total defect effect depends on all spatial components jointly. Future quantitative work would require amplitude-density analysis and regularization-artifact correction; here, the focus is on successful localization from sparse data.



(a) CFRP plate response at $t = 0.17$ ms, bandpass filtered to 1–50 kHz. Transducer 5 is active. Compared to the unfiltered snapshot in Figure 2, the pulse is significantly broadened due to the lowpass filtering.

(b) Same setup at $t = 1.9$ ms, near the end of the 2 ms period. The pulse tail from the current repetition is still visible, and the pulse from the next repetition (nominally starting at $t = 0.12$ ms) is already present, demonstrating the wraparound inherent in the periodic time treatment.

Figure 7: Effect of 1–50 kHz bandpass filtering on the transducer pulse shape in the periodic time framework.

Working effectively in the 1–50 kHz band validates the empirical operator concept, even with practical imperfections such as pulse shape drift and measurement misalignment. The robustness in this band supports our initial hypothesis; circumventing detailed forward models in favor of empirical operators leads to numerically robust properties in the detection algorithm, allowing imperfections to be absorbed into the interpretation of the measured quantities themselves. By removing the concept of spacial dimensions entirely (as the algorithm does not know about the spatial relations between each grid point) it naturally removes restrictions caused by the the frequency to pulse width relations, allowing us to work in low frequencies, which in turn leads to numerical robustness.

6. Conclusion

A. My Appendix

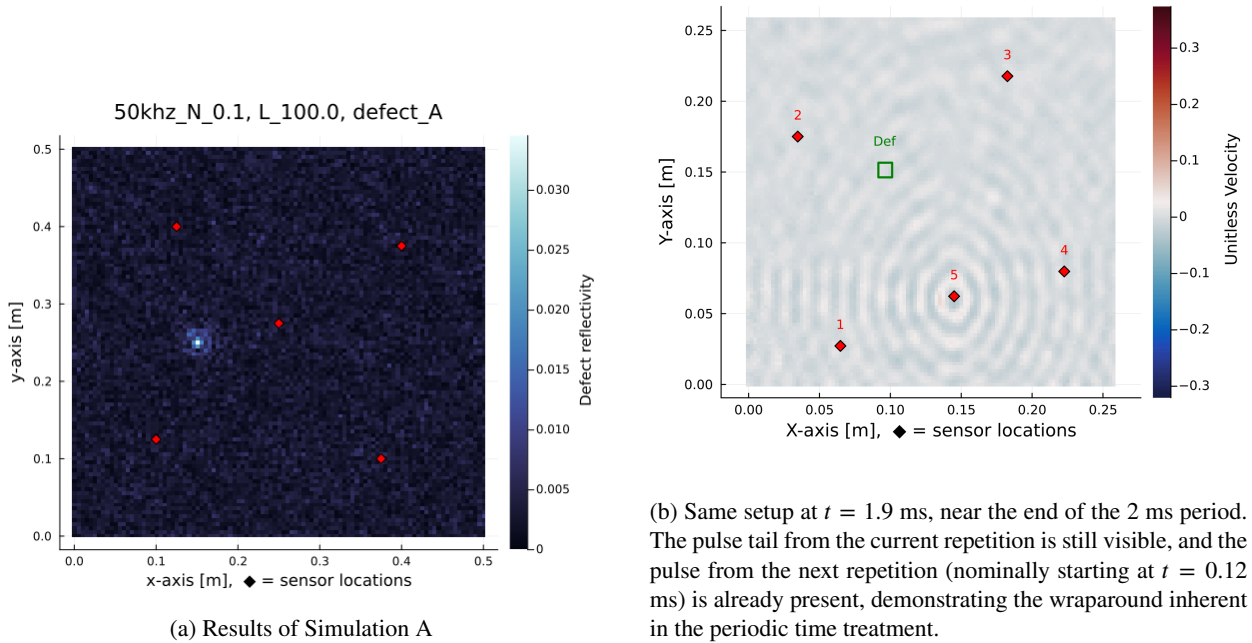
A.1. Low Frequency data

The results presented in the main paper employ a 1–50 kHz bandpass filter, which differs significantly from the unfiltered calibration data shown in Figure 2. Figure 7a shows the same acquisition time point, but after lowpass filtering to 50 kHz. The pulse duration expands dramatically, becoming so long that it wraps around within the periodic time window. At the end of the 2 ms period ($t \approx 1.9$ ms), the pulse from the next repetition is already visible (Figure 7b). This behavior illustrates a key strength of the framework: the algorithm does not require short, well-separated pulses. Instead, it relies on the imposed periodicity and the circulant operator structure, which naturally accommodate extended pulse durations. The periodic time treatment is therefore not merely a computational convenience but is fundamentally embedded in the mathematics of the inverse problem.

A.2. Previous Results based on Simulations

In a previous work leading up to this paper, extensive testing of the same method based on simulations has been performed. Using commercial simulation software, the method has been tested against various defects using a rectangular aluminum plate of 9mm thickness. Defects have been simulated using changes in density on the plate. The two such results are shown in Figures TODO. The simulated results show somewhat similar pattern to that of the real worls simulations. The main difference being that the results do not degrade with higher frequency bands, and no

Raw data with emitter 5 at time 1.9 ms

**Figure 8:** Defect A, a heatmap of the densities on the aluminum plate.

exclusion zones are required aside from the sensor locations themselves. (Even in simulations, there have been relative pulse amplitude variations of the order of 0.05-0.2 for reasons we cannot quite explain).

A.3. Discussions regarding validity of the Dispersion curve

Figures 3 indicate phase velocities approaching 6km/s or higher as the frequency increases. Using theoretical lamb isotropic wave analysis using rough estimates of the densities of CFRP plates, we obtain that the A0 mode converges towards roughly 3.8km/s as the frequency increases. The empirical numbers are within a reasonable range to the model in comparison, albeit I personally am taking the empirical numbers with care. Given we only use the phase velocities to judge whether the method did achieve sub wavelength localization, the exact numbers are not highly important, so it is likely safe to say that the phase velocities at 50khz are in the range of 4-8cm depending on direction. Even in this case, the localization accuracy at roughly 2cm is well below the wavelengths involved. Therefore no further study into the velocities are made.

A.4. Regarding Frequencies and reconstruction

The algorithm appears to have decreased benefit from using higher frequency data, despite the frequency spectrum of the waves going well over 50khz, which is expected given the central frequency of 80kHz of the pulses sent, but is also confirmed by analyzing the responses at various locations on the plate. This deviates from a previous simulation study where the same method was tested in a simulated environment. As discussed in section 5, the misalignment of the measuring location at the sensors is likely a factor at higher frequencies. Another reason may lie in the fundamental assumption in how the problem is set up. In section 3.5 we introduce a simplified assumption in that a defect responds in a delta like manner, meaning incoming waves are reflected instantly, with no phase dependence. In the simulation study, defects were modeled as changes in density, while the real work example through an adhered metal cube is more similar to a change in stiffness. It may be that in the latter case, the assumption of frequency independent responses is less valid. In that case, restricting the frequency band may be helpful in that, while the data available is decreased, the frequency region in which the assumption has to be valid is decreased, making the assumption valid in more situations. Given the experiment performed, we cannot isolate these variables to give a definitive answer.

A.5. Piezoelectric Measuring

A full transducer based implementation may be to be done as follows:

For every transducer location, use two transducers close by: One is the transmitting transducer, and the other the sensing one. During calibration, one of the transmitting transducers sends out a periodic pulse, and an ldv scans the object in the experiemnt of this paper. In addition to the LDV data, the sensing transducers's measurements are also added to the LDV data, and is treated as a grid point as any other. In the code, treat the sensing transducer measurement as that of the emitter location. This way, all problems regarding coupling when the transducer is measuring is absorbed into the the object properties, and should allow the use of cheap transducers with poor coupling properties.

Notes: Do not use thick transducers, such as ones with the shape of a cube for this application. The thickness increases stiffness of the plate locally, making measurement on and by the transducer impossible. Always use flat transducers relative to plate thickness such as ceramic based transducers.

One may notice that the actual location of the emitting transducer, and that which is considered the transmitter is not the same. This is fine and intentional, and is implicitly done in this paper as well, since the LDV does not scan exactly at the locations where the transducers are adhered, and is mathematically consistent. One may think we could decouple the locations of the actual transducer, and the transducer location even further, but it quickly becomes highly unstable at a few cm of distance. There is however a possibility to use one emitting transducer, and multiple sensing transducer close by, treating every sensing transducer as an emitter in the model. I hypothesize this could work, but the benefit may be diminishing.

A.6. Computational aspects

Due to the large amounts of data involved, it is necessary to save intermediate data to disk and load sections as needed. The HDF5 file format is useful for this application.

The Tikhonov inversion in (16) has been implemented by explicitly computing the matrix term and saving it. While this allows future measurements to use only a fast matrix multiplication, for increasingly large sizes it may become necessary to compute the result iteratively and out of core.

A.7. Generalization to arbitrary defect bases

As mentioned in Section 3.5 and applied in Section 3.6, we assumed the defect to act as a perfect reflector of form \vec{e}_0 . In general this assumption does not hold for more complicated defects, such as delaminations in fiber-reinforced materials. In this case, using a simulation with a defect at a known location, one can compute the response nature through similar means to those described in Sections 3.6 and 3.7. Assuming we have obtained empirical defect vectors for two defect types of interest, \vec{b}_1 and \vec{b}_2 , we can implement these two vectors as a basis using a projector matrix P :

$$P := \begin{bmatrix} \vec{b}_1 & \vec{b}_2 \end{bmatrix} \quad (17)$$

Replacing \vec{e}_0 in 12, we obtain

$$L_{ij} := [G_{i1}G_{1j}S_jP \mid G_{i2}G_{2j}S_jP \mid \dots \mid G_{iN}G_{Nj}S_jP], \quad (18)$$

as well as an adjustment to the full defect vector \mathbf{d} to hold two parameters per location.

$$\mathbf{d} := \begin{bmatrix} d_{1,1} \\ d_{1,2} \\ d_{2,1} \\ \vdots \\ d_{N,2} \end{bmatrix} \quad (19)$$

where for $d_{k,b}$, k denotes the grid location, and b the basis vector at that location.

References

- [1] Chen, S., Thompson, A., Dodwell, T., Hallett, S., Belnoue, J., 2025. A comparison between robust design and digital twin approaches for non-crimp fabric (ncf) forming. Composites Part A: Applied Science and Manufacturing 193, 108864. URL: <https://www.sciencedirect.com/science/article/pii/S1359835X25001587>, doi:<https://doi.org/10.1016/j.compositesa.2025.108864>.

- [2] Ebrahimpour, A., Salamone, S., 2017. Acoustic emission source localization in thin metallic plates: A single-sensor approach based on multimodal edge reflections. *Ultrasonics* 78, 134–145. doi:10.1016/j.ultras.2017.03.006.
- [3] Han, S., Li, Q., Cui, Z., Xiao, P., Miao, Y., Chen, L., Li, Y., 2024. Non-destructive testing and structural health monitoring technologies for carbon fiber reinforced polymers: a review. *Nondestructive Testing and Evaluation* 39, 725–761. URL: <https://doi.org/10.1080/10589759.2024.2324149>.
- [4] Kosova, F., Özkan Altay, Özgür Ünver, H., 2025. Structural health monitoring in aviation: a comprehensive review and future directions for machine learning. *Nondestructive Testing and Evaluation* 40, 1–60. URL: <https://doi.org/10.1080/10589759.2024.2350575>, doi:10.1080/10589759.2024.2350575, arXiv:<https://doi.org/10.1080/10589759.2024.2350575>.
- [5] Tikhonov, A.N., 1963. On the solution of ill-posed problems and the method of regularization. *Dokl. Akad. Nauk SSSR* 151, 501–504. URL: <https://www.mathnet.ru/eng/dan/v151/i3/p501>. english translation available via MathNet.Ru.
- [6] Wan, L., Ismail, Y., Sheng, Y., Ye, J., Yang, D., 2023. A review on micromechanical modelling of progressive failure in unidirectional fibre-reinforced composites. *Composites Part C: Open Access* 10, 100348. URL: <https://www.sciencedirect.com/science/article/pii/S266668202300004X>, doi:<https://doi.org/10.1016/j.jcomc.2023.100348>.